



Fe–N supported on graphitic carbon nano-networks grown from cobalt as oxygen reduction catalysts for low-temperature fuel cells

Emanuela Negro^{a,*}, Alessandro H.A. Monteverde Videla^b, Vincenzo Baglio^c,
Antonino S. Aricò^c, Stefania Specchia^{b,**}, Ger J.M. Koper^a

^a Delft University of Technology, Department of Chemical Engineering, Julianalaan 136, 2628BL Delft, The Netherlands

^b Politecnico di Torino, Department of Applied Science and Technology, Corso Duca degli Abruzzi 24, 10129 Torino, Italy

^c Consiglio Nazionale delle Ricerche, Istituto di Tecnologie Avanzate per l'Energia "Nicola Giordano", Salita S. Lucia sopra Contesse 5, 98126 Messina, Italy

ARTICLE INFO

Article history:

Received 27 June 2014

Received in revised form 21 October 2014

Accepted 29 October 2014

Available online 3 November 2014

Keywords:

Iron–nitrogen electrocatalyst

Carbon nano-networks

PEM fuel cells

Direct methanol fuel cells

Oxygen reduction reaction.

ABSTRACT

Three iron–nitrogen-containing non-noble metal electrocatalysts supported on networked graphitic structures, carbon nano-networks (CNNs), were synthesized using a wet-impregnation method. The CNN supports were produced in-house by chemical vapor deposition of ethene over cobalt nanoparticles that were previously synthesized in bicontinuous microemulsions. The three CNN supports differed in cobalt content, ranging from 0.1 to 1.7% in weight. These CNN supports were used to prepare Fe–N/CNN electrocatalysts. The oxygen reduction reaction (ORR) activity was evaluated by rotating disk electrode measurements. Interestingly, the highest ORR activity belonged to the catalyst with the highest iron and cobalt content. The most promising catalyst was investigated as the cathode material in a polymer electrolyte membrane fuel cell (PEMFC) and a direct methanol fuel cell (DMFC). The maximum recorded power densities were 121 mW cm^{−2} for PEMFC and 15 mW cm^{−2} for DMFC, respectively. These values are superior or comparable to the best state of the art for similar materials. The durability to potential cycling was tested in half-cell studies and an activity loss around 10% was found after 1000 cycles, which is not significantly different from what is reported in the literature. The relatively simple synthesis approach and the cheap precursor materials make this electrocatalyst promising for low-temperature fuel cell applications.

© 2014 Elsevier B.V. All rights reserved.

1. Introduction

Low-temperature fuel cells, such as PEMFCs and DMFCs, are very promising energy conversion devices for future sustainable and distributed energy generation both for mobile, portable and stationary applications because of their high efficiency and low CO₂ emission [1,2]. However, the main issues preventing mass-scale commercialization of such devices are their cost and durability that are not meeting worldwide requirements. These issues are closely related to the FC electrodes [3], currently consisting of platinum nanoparticles (NPs) loaded onto high-surface-area carbon supports, such as carbon black.

The high cost is mainly associated to the use of platinum as necessary for the ORR at the cathode [4]. Efforts have been done

to decrease the cost of the catalyst by replacing platinum with non-noble metals [5]. Since Van Veen *et al.* [6], Scherson *et al.* [7] and Wiesener *et al.* [8] discovered that transition metals, such as Co and Fe with porphyrins, phthalocyanines and chelates supported on carbon and subjected to heat treatment were characterized by interesting ORR activity under acidic conditions, many efforts have been done to increase the performance of non-noble metal catalysts to reach at least 1/10 of platinum mass activity values [9–19]. Pyrolysis plays a crucial role in the creation of active sites where the transition metal is usually linked to nitrogen and carbon as M–N₂–C and M–N₄–C, to promote the reduction of oxygen under acid conditions [3–5]. In order to form an active site, nitrogen must be introduced into the graphene layer of carbon. Carbon–nitrogen catalysts exhibit electrocatalytic activity due to the unique electronic interactions between the lone-pair electrons of nitrogen and the p-system of graphitic carbon. Unfortunately, most of the explored heat-treated non-noble metal–nitrogen catalysts show relatively low activity and stability compared to Pt-based catalysts in the acidic operating environment of a real fuel cell [20]. Recently, Lefevre *et al.* [14], Wu *et al.* [15] and Cheon

* Corresponding author. Tel.: +31 0 15 2786181.

** Corresponding author. Tel.: +39 011 0904608.

E-mail addresses: e.negro@tudelft.nl (E. Negro), stefania.specchia@polito.it (S. Specchia).

et al. [21] studied different ways to create and dope transition metals with nitrogen in the carbon framework, obtaining the highest performance reported so far.

The low durability of the conventional Pt-based electrode materials is due to several phenomena, such as catalyst particle aggregation and dissolution, which take place especially in non-ideal conditions such as potential and temperature cycling and fuel starvation [22]. The major degradation mechanism has been identified in carbon corrosion at high potentials (>0.8 V vs. RHE). Carbon corrosion can cause, among others, loss of hydrophobicity leading to electrode flooding, catalyst detachment leading to loss of electrochemically active surface area, loss of porosity, with consequent mass transport problems. The use of graphitic carbon materials such as carbon nanotubes (CNTs), carbon nanofibers (CNFs) and graphene has been proven to be beneficial for electrode durability since sp^2 -hybridized carbon is less prone to oxidation [3,23–26].

Within the TU Delft group, we developed a novel carbon material that consists of networked carbon nanostructures (CNNs), currently produced by the TU Delft spin-off company CarbonX [27]. CNNs are 3D hyper-branched carbon graphitic structures organized in a nanoscale pattern. They can be easily produced by CVD of ethene over transition metal catalyst, used as nucleation elements, synthesized in bicontinuous microemulsions (BME) [28,29]. The formation of networked, sponge-like, carbon graphitic structures is due to the carbonization of the surfactant, being the primary carbon source. CNNs show attractive properties for catalysis in fuel cells, such as high specific surface area, micro- and meso-porosity, high electrical conductivity, great oxidation resistance and surface defects, increasing the material ability to disperse in solution and to simplify integration into polymer matrices [27,30]. Previous studies showed that CNNs can be successfully used as a more durable support for platinum catalysts for ORR compared to commercially used carbon supports, while their performance is comparable to that of CNTs [26]. The versatility and simplicity of the synthesis route promises a less expensive production than CNTs.

Here, we report on three different types of CNNs synthesized by varying the quantity of Co from 0.1 to 1.7% in weight and used as novel carbon support of non-noble Fe–N electrocatalyst [31,32] for the oxygen reduction reaction in PEMFC and DMFC.

2. Experimental

2.1. Chemicals

Sodium bis(2-ethylhexyl)sulfosuccinate as surfactant, also known as Na-AOT ($C_{20}H_{37}NaO_7S$, 99%), *n*-heptane (99.9%) as solvent, cobalt acetate tetrahydrate ($(CH_3COO)_2Co \cdot 4H_2O$, 99.999%) as metal precursor, sodium borohydride (granular, $\geq 98\%$) as reducing agent, 2,3,5,6-tetrakis(2-pyridyl)pyrazine (TPTZ, 97%) as nitrogen source, isopropanol (99.5%), ethanol (99.5%), methanol (MeOH, 99.8%), sulfuric acid (97–98%) were purchased from Sigma-Aldrich. Iron(II) acetate (FeAc, 97%) metal source was purchased from Strem Chemicals. Ethene, nitrogen, hydrogen and oxygen gases were supplied in cylinders by Siad with 99.999% purity. Hydrochloric acid solution (1.0 M), Nafion® solution in aliphatic alcohols (5%) and anodic PtRu catalyst (1:1 at.%) were purchased from Alpha Aesar. All aqueous solutions were prepared using ultrapure water obtained from a Millipore Milli-Q system with resistivity $>18 M\Omega cm^{-1}$. All chemicals were used as-received from suppliers.

2.2. Carbon support and electrocatalyst synthesis

2.2.1. Preparation of CNNs

Three batches of CNNs, labeled CNN1, CNN2 and CNN3, were synthesized by catalytic CVD, as previously described [27,30].

Briefly, we performed a fixed-bed thermal catalytic CVD at $700^\circ C$ of ethene over cobalt (Co) NPs prepared in BMEs and subsequently loaded into a ceramic vessel. Co NPs were synthesized in BME containing water/Na-AOT/*n*-heptane in 0.2/0.54/0.26 weight ratios as described elsewhere [28,29]. Co NPs were characterized by dynamic light scattering (DLS) and transmission electron microscopy (TEM). Raman spectroscopy, scanning electron microscopy (SEM), energy-dispersive X-ray spectroscopy (EDX) and TEM were carried out to characterize the carbon support.

2.3. Preparation of Fe–N/CNNs

Electrocatalysts were synthesized as previously described [31,32]. Briefly, CNN1, CNN2 and CNN3 were impregnated using TPTZ as nitrogen source and iron acetate as iron source, with a molar ratio equal to Fe/TPTZ 1:6. After 24 h impregnation, pyrolysis was performed, under nitrogen atmosphere at $900^\circ C$ for 3 h [31,33,34]. The powder was collected, grounded and acid-treated at $80^\circ C$ under reflux bath, in order to remove any possible iron oxide or its instable compounds, or metallic iron [33,35]. Raman spectroscopy, X-ray photoelectron spectroscopy (XPS), TEM and EDX were carried out to further characterize the electrocatalysts, herein after called Fe–N/CNN1, Fe–N/CNN2 and Fe–N/CNN3.

2.4. Support and electrocatalyst characterization

We performed DLS on the Zetasizer Nano ZS from Malvern Instruments Ltd. Samples were diluted 20 times in heptane and sonicated for 1 hour before the measurements.

Nitrogen adsorption isotherms were recorded by an ASAP 2020 Instrument (Micromeritics) at 77 K. Before the analysis, all the samples were placed into the cell and degassed under vacuum for 3 h at $150^\circ C$. The specific surface area of the samples was calculated using the Brunauer–Emmett–Teller (BET) method within the relative pressure range of 0–1. The pore size volume was obtained with the Barrett–Joyner–Halenda (BJH) method.

TEM was carried out using two electron microscopes: an FEI Monochromated Tecnai 200STEM-FEG operated at 200 kV, in which images were acquired with a Gatan CCD camera, and a Philips CM300UT-FEG with a point resolution of 0.17 nm, information limit of 0.1 nm, also operated at 200 kV, in which images were acquired with TVIPS CCD camera. Measurements of NPs in BMEs were prepared by immersing a Quantifoil R copper microgrid first in the microemulsion containing the NPs and afterwards in acetone to wash away part of the surfactant. Measurements of CNNs were prepared by immersing a Quantifoil R copper microgrid in a dispersion of CNNs in ethanol ($1 mg mL^{-1}$). Elemental analysis by means of EDX was carried out during TEM measurements.

SEM was conducted with a XL20 microscope from Philips Electronics N.V. having a tungsten filament operated at 15 kV as source of electrons. For CNNs, samples were attached to a carbon conductive tape and subsequently to the aluminum sample holder. For SEM and EDX of Fe–N/CNNs, we used JSM-6010LA microscope from JEOL. The catalyst was previously dispersed in ethanol, and a droplet was loaded over a silicon support and let it to dry. Raman spectroscopy was performed using a Raman imaging microscope, System 2000 from Renishaw Public Limited Company. The instrument was operated with a 20 mW argon laser of wavelength 514 nm and calibrated using a silicon wafer. All spectra were taken with at 10 s collection time at approximately $1 cm^{-1}$ resolution. They were subsequently normalized to the maximum intensity.

XPS measurements were carried out on Fe–N/CNNs using a Physical Electronics PHI 5800 (USA) multi-technique ESCA system (with monochromatic Al K α X-ray radiation source at 1486.60 eV). The survey and narrow spectra were obtained using different pass

energy [36]. The samples were placed in an ultrahigh vacuum chamber at 5×10^{-10} Torr and calibrated against a value of the C 1s binding energy of 284.5 eV. Multipak 9.0 software was used for obtaining semi-quantitative atomic percentage compositions, using Gauss–Lorentz equations with Shirley background.

2.5. Electrochemical characterization

Electrocatalysts activity was evaluated through linear sweep voltammetry (LSV) in a three-electrode electrochemical cell using a rotating disk electrode (RDE) instrument (RRDE-3A ALS Model 2323), and bi-potentiostat (CH Instrument Model 760). A catalyst-coated glassy carbon disk electrode with a geometric area of 0.1257 cm^2 was used as working electrode, platinum wire as the counter electrode and an Ag/AgCl as reference electrode, respectively. All of the electrode potentials were corrected and referred to the standard hydrogen electrode (SHE). Oxygen and nitrogen were purged for 40 min before all tests. 10 mg of catalyst was dispersed in 45 μL of 5% Nafion in ethanol which corresponds to a Nafion to carbon ratio equal to 0.2 [32]. The ink was sonicated for 40 min. Finally, $500 \mu\text{g cm}^{-2}$ were deposited on the working electrode, which was dried overnight. Background current was measured by running cyclic voltammetry at 10 mV s^{-1} in N_2 -purged $0.5 \text{ M H}_2\text{SO}_4$ to account for capacitive current contributions. The background current was then subtracted from the experimental ORR current to eliminate any contribution of capacitive current. LSV was performed at 1600 rpm in O_2 -saturated $0.5 \text{ M H}_2\text{SO}_4$ solution at room temperature and kinetic currents were evaluated at 800 mV vs. RHE.

Half-cell tests were carried out in a three-electrode cell consisting in a gas diffusion electrode as working electrode, a mercury-mercurous sulfate ($\text{Hg/Hg}_2\text{SO}_4$, sat.) as reference electrode and a platinum grid as counter electrode. The gas diffusion electrode was prepared according to a procedure described in previous work [25]. Briefly, hydrophobic carbon cloth (LT 1200 W Elat, ETEK) was used as backing layer on which the catalytic layer was distributed with a blade. The catalytic layer was composed of 33% Nafion and 67% wt. catalyst. Catalyst loading was 1.6 mg cm^{-2} . The electrode area was 1.5 cm^2 and $0.5 \text{ M H}_2\text{SO}_4$ solution was used as electrolyte. Gases (oxygen or nitrogen) were fed from the backside of the electrode in order to perform electrochemical test as described. An Autolab Metrohm potentiostat/galvanostat was used to perform the measurements. Accelerated durability tests (ADTs) were carried out by scanning the potential between 0.6 and 1.2 V at a scan rate of 20 mV s^{-1} in $0.5 \text{ M H}_2\text{SO}_4$ saturated with N_2 by performing 1000 cycles [25]. Uncompensated resistance was obtained from high-frequency impedance. Cyclic voltammetry (CV) was carried out before and after ADT at room temperature, 25°C , with a scan rate of 50 mV s^{-1} in a potential window of 0.02–1.2 V vs RHE.

ORR activities before and after ADT were evaluated by means of the LSV at 10 mV s^{-1} between the OCV and 0.1 V vs RHE.

For single-cell studies, electrodes were prepared as for half-cell studies. Catalyst loading was 2.6 mg cm^{-2} for the non-noble metal cathode and 2.6 mg cm^{-2} for commercial PtRu 1:1 at.% anode. The membrane electrode assemblies (MEAs) for single-cell studies were prepared by hot-bonding the electrodes on either side of a pre-treated Nafion® 115 membrane at 130°C and $50 \text{ kg}_\text{F} \text{ cm}^{-2}$. Single-cell tests were performed in a fuel cell test fixture of 5 cm^2 active area (Hydrogenics Test Systems). For single-cell polarization experiments, H_2 (RH 100%) or MeOH (1, 2 or 10 M) and O_2 (RH 100%) were fed, respectively, to the anode and cathode chamber.

3. Results and discussion

3.1. Physical–chemical characterization of supports and electrocatalysts

Co NPs were synthesized in BMEs in different concentrations, ranging from 10 to 100 mM of Co precursor dissolved in the water phase. Higher concentrations result in unstable catalyst NPs that sediments with time, due to high ionic strength causing the decomposition of the matrix as reported previously [28,29]. The size of NPs, stabilized by Na-AOT, measured with DLS is $4.2 \pm 0.8 \text{ nm}$ (Fig. 1a). From this, an effective size of 2 nm for the NPs is estimated, taking into account the length of surfactant molecules absorbed on the surface of the particle [28,29]. This estimation is confirmed by TEM measurements (Fig. 1b). Narrow size distributions of NPs are crucial for the synthesis of CNNs resulting in homogeneous structures. The use of large amount of surfactant prevents the massive aggregation of colloidal metal particles [28,29].

BME containing Co was loaded into a ceramic vessel and three batches of CNNs were in-house produced from the decomposition of ethene at 700°C . Batches differ in Co content and in the graphitic nature of the structure, as reported in Table 1. The Co content in the carbon structure was estimated from a mass balance and varied from 0.1% to a maximum of 1.7%, depending on the NP concentration of the BME precursor.

TEM and SEM images of the synthesized carbon supports are displayed in Fig. 2. The CNNs show a sponge-like isotropic morphology consisting of networked graphitic nanosheets. The formation of networked, sponge-like and carbon graphitic structures is due to the carbonization of the surfactant, being the primary carbon source [27,30]. The thickness of carbon nanostructures varies with Co concentration. At low amounts of Co NPs in the BME, corresponding to 0.1% in the final structure, thicker structures (Fig. 2a and d) are obtained due to a limited amount of nucleation points for graphitic carbon. Increasing Co concentrations to 0.8% in the final structure led to thinner CNNs due to an increased number of

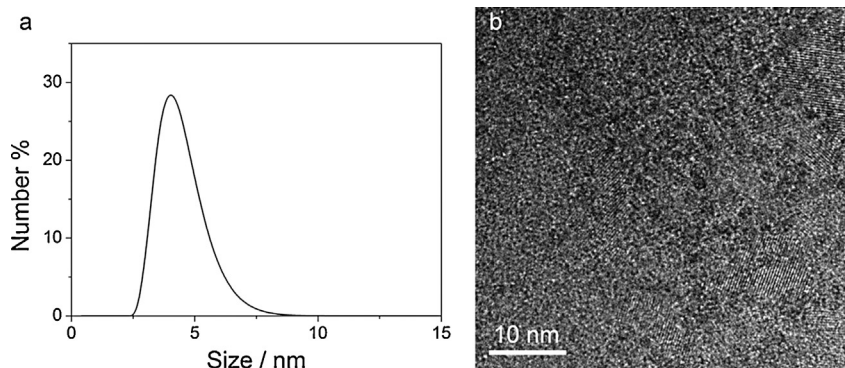


Fig. 1. (a) Co NPs size distribution from DLS measurements and (b) TEM image of Co NPs synthesized in BME and diluted 20 times.

Table 1
Supports and electrocatalysts physical–chemical properties from mass balance and Raman analyses.

	Cobalt (wt%) (before Fe–N deposition)	I_D/I_G (before Fe–N deposition) supports	I_D/I_G (after Fe–N deposition)
CNN1	0.1	0.78	0.84
CNN2	0.8	0.66	0.85
CNN3	1.7	0.80	0.90

nucleation points at equal amount of carbon precursor (Fig. 2b and e). With a further increase in Co concentration up to 1.7% in the final structure yielded slightly thicker CNNs mainly because of the simultaneous growth of carbon sheets due to the high density of catalyst NPs (Fig. 2c and f) [27,30].

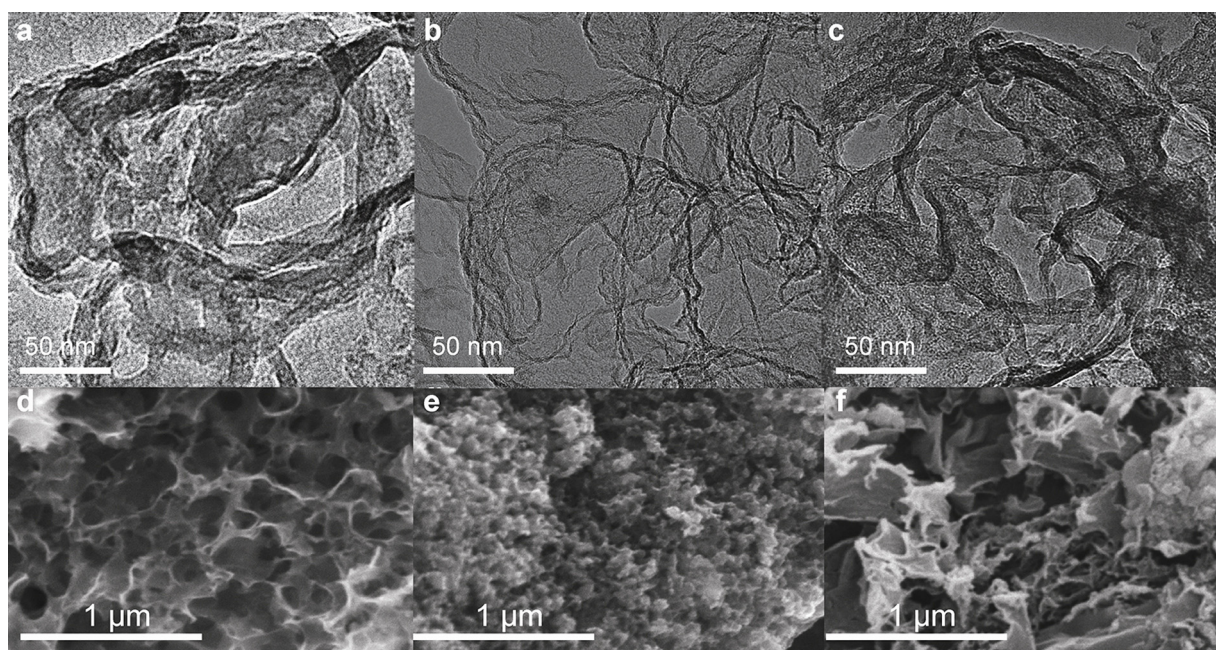
The BET specific surface area of all the CNN supports are very similar among them, ranging between 72 and 74 m² g^{−1}, whereas these values slightly decrease to 61–62 m² g^{−1} for the Fe–N/CNN catalysts, presenting a total BJH pore volume close to 0.54 cm³ g^{−1} and a micropore volume close to 0.01 cm³ g^{−1}.

These results are complemented by those from Raman spectroscopy on the different samples (see Fig. 3). From the ratio between the intensity of the D band at circa 1350 cm^{−1} and the G band at circa 1580 cm^{−1}, the ratio between the disordered and the graphitic carbon structure is estimated [37]; values are reported in Table 1 as I_D/I_G . The influence of Co on graphitization and disorder was quantified as follows. Defects are present in the structure because of two reasons: (i) the presence of heteroatoms in the sp² structure or of sp³-hybridized carbon atoms and (ii) the presence of Co and nucleation points and thus junctions close to which the amount of defects is higher compared to elongated structures [26,27,30]. A low Co content leads to a low nucleation site concentration such as in CNN1 which turns out not to be sufficient to favor the transformation of all of the carbon from the surfactant and the hydrocarbon feed into graphitic sheets, and subsequently results in a high level of defects with an I_D/I_G ratio of 0.78 which is mainly due to sp³-hybridized carbon. When using a higher amount of Co, as in CNN2, the level of defects decreases, I_D/I_G ratio equal to 0.66, due to the higher amount of graphitized carbon. In CNN3, the amount of defects has increased further, leading to an I_D/I_G ratio equal to 0.80 because of the larger amounts of nucleation points and thus of networks, where mainly sp³ carbon is found [27,30].

After the next step where the electrocatalysts are deposited, the I_D/I_G ratio from Raman measurements increases for all the supports reaching similar values, ranging from 0.84 to 0.90. During the electrocatalyst synthesis, two phenomena occur. At high temperature, under inert atmosphere, further graphitization of the carbon takes place. This is clearly visible in Fig. 3 from the shift of the G band towards lower wavenumbers [37,38], occurring in all the electrocatalysts synthesized. Further graphitization would lead to a lower amount of defects and thus a lower I_D/I_G ratio [37]. However, carbon is simultaneously doped with nitrogen, which causes a broadening of D and G peaks as can be seen in Fig. 3, meaning that the fraction of defects in the carbon phase in the material is increased [39]. This would lead to an increase of the I_D/I_G ratio. Thus, the final increase of the I_D/I_G ratio is the net effect of the sum of its decrease due to further graphitization and its increase due to nitrogen introduction in the structure, which is the major contribution.

Indeed, from XPS measurements reported in Table 2, for Fe–N/CNN2, we have the higher amount of N introduced in the structure, corresponding to the higher net increase in the D and G bands (see Table 1). This is in agreement with our previous argument: CNN2 has a lower amount of defects due to the higher level of graphitization of the carbon, so that the amount of defects increases just due to the introduction of nitrogen in the structure. For CNN1 and CNN3 instead, during the electrocatalyst synthesis, the amount of defects increases because of nitrogen introduction but decreases because more defected carbon is converted into graphitic carbon, resulting in a lower net increase of the bands.

Morphological structure, graphitization and degree of disorder are influenced by the content of Co, as described above. Previous studies showed that during pyrolysis, transition metals can both promote nitrogen fixation in the carbon frameworks and contribute

**Fig. 2.** TEM images of samples labeled: (a) CNN1, (b) CNN2, (c) CNN3, with SEM images (d) CNN1, (e) CNN2 and (f) CNN3.

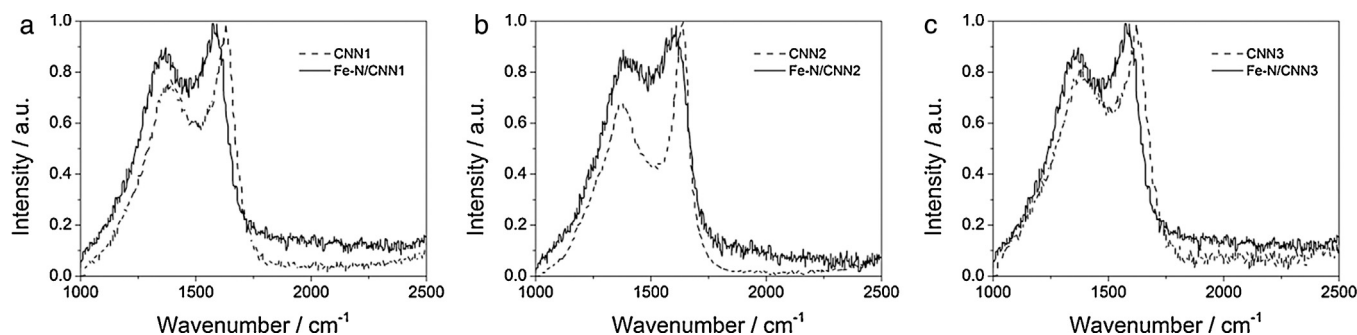


Fig. 3. Raman spectra of CNNs and of the respective Fe-N/CNN electrocatalysts.

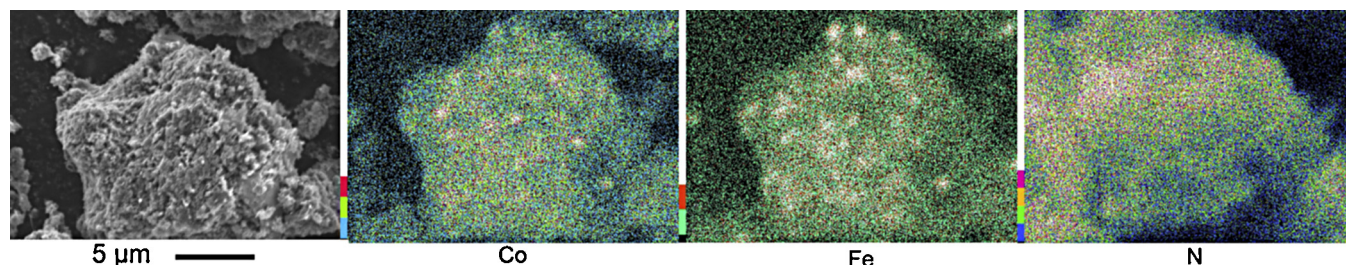


Fig. 4. SEM image and EDX mapping for Fe-N/CNN3.

to further graphitization of the carbon [13,40]. In the latter case, transition metal encapsulation by carbon was observed [40].

Table 2 reports iron and cobalt content in Fe-N/CNNs calculated from EDX after acid washing. The amount of iron in electrocatalysts structure slightly increases from CNN1 to CNN3. Since the values of Fe are higher than what observed in the literature for similar studies [9,13], we explained these results by supposing that CNN supports uses part of the iron to promote graphitization of the carbon [13]. Cobalt is measured only in the Fe-N/CNN3 catalyst, being the Co amount in the other two catalysts below the limit of detections of the machine (1% in weight). Fe-N/CNN3 derives, in fact, from the CNN3 support prepared from the microemulsion containing the highest Co content (1.7 wt%) (see Table 1).

Fig. 4 shows the EDX map of Fe-N/CNN3 electrocatalyst, where the distribution of the functionalizing elements Fe and N, as well as Co and oxygen can be observed. EDX spectrum and maps for Fe-N/CNN1 and Fe-N/CNN2 are given in Fig. S1 in the Supporting Information (SI). Interestingly, Fe-rich sites overlap with the Co-rich sites being the nucleation sites where network junctions, richer in defects, are located as described above. In agreement with our results, previous studies show that highly defected carbon is more easily functionalized for which reason the nitrogen content in the electrocatalyst as well as their activity is directly proportional to the amount of defects in the initial carbon structure [41,42].

Table 2 reports the surface compositions of the electrocatalyst as measured by XPS. The surface nitrogen was higher in CNN2, 6.2% and CNN3, 5.7%, than in CNN1, 4.2%. According to what discussed

above, CNN1 might encapsulate part of iron to promote further graphitization, and thus a lower amount of iron is available to promote nitrogen introduction [43]. Another possibility is that Co plays an active role in promoting the introduction of nitrogen into the structure [44–47]. This hypothesis would assume that the Co particles are partially exposed to the external environment and not completely enclosed by the graphitic carbon. However, in previous studies, the Co NPs were shown to be encapsulated by the carbon [26].

Fig. 5 shows the high-resolution XPS nitrogen spectra of the prepared catalyst. The corresponding wide scan spectra are given in Fig. S2 of the SI. The results of the deconvolution of the spectra, with N percentages and binding energy values reported in Table 2, show three different nitrogen peaks originating from pyridinic nitrogen (N1: nitrogen atoms are bound to two carbon atoms located at the edges or defect sites and contributes to the π system with one p-electron), pyrrolic nitrogen (N2: the sp^2 -hybridized nitrogen is part of a five-member ring structure, or lactam groups) and quaternary graphite-like nitrogen (N3: nitrogen atoms are incorporated into the carbon structure substituting a carbon atom) [48,49]. In our samples, the pyridinic oxide-N (N4 at 402–405 eV, which includes intercalated nitrogen molecules: it refers to a π - π^* shake-up satellite peak) is not present. N1, N2 and N3 are present in all of the prepared samples. Interestingly, the N3 content is similar for all of the three electrocatalysts, whereas N1 and N2 contents have different trends: high N1 content and low N2 content for CNN1, low N1 content and high N2 content for

Table 2
Bulk elemental quantification of Co and Fe from EDX.

	EDX (at.%)	XPS (at.%; eV)					
	Co	Fe	N	N1	N2	N3	N4
Fe-N/CNN1	n.d. ^a	0.27	4.3	57; 398.68	13; 399.84	30; 401.05	0
Fe-N/CNN2	n.d. ^a	0.30	6.2	4; 397.88	71; 398.53	25; 400.80	0
Fe-N/CNN3	0.52	0.38	5.7	36; 398.33	28; 399.30	36; 400.95	0

Surface composition from XPS spectra and their nitrogen convolution analysis on Fe-N-based electrocatalysts (N1: pyridinic N; N2: pyrrolic and/or cyanide-like N; N3: quaternary graphite-like N; N4: N oxides, nitro or nitrous groups, of pyridine).

^a Non-detectable.

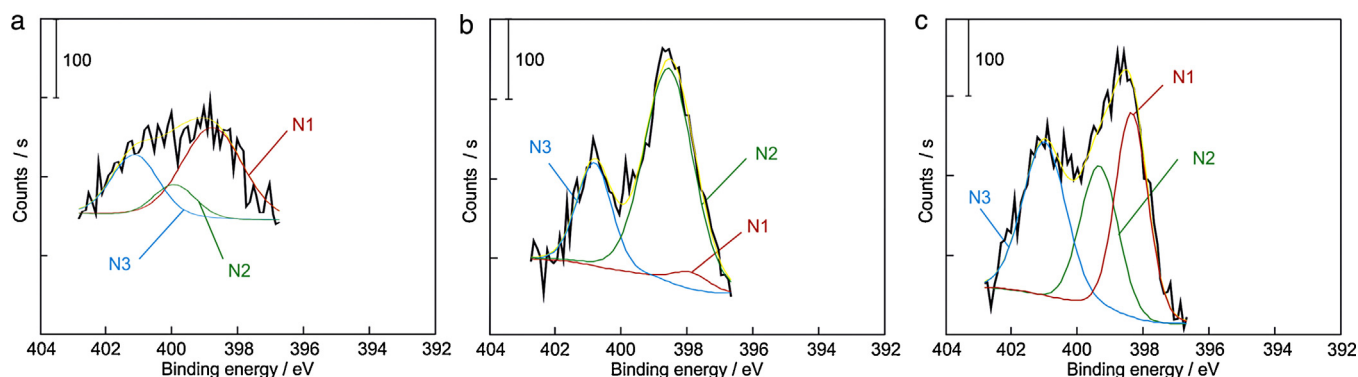


Fig. 5. Deconvolution of the high-resolution XPS spectra of N 1s for Fe-N/CNN1 (a), Fe-N/CNN2 (b), and Fe-N/CNN3 (c).

CNN2, and similar N1-N2 contents for CNN3 sample. According to the literature, the electrocatalytic ORR activity can be attributed to N1 or N2 [7,35,50–52], although other authors suggested that N3 was more important for the electrocatalytic activity of N-doped carbon-based electrocatalysts [53–55]. Furthermore, the presence of stable N3 graphitic-like groups could lead to a relatively stable electrocatalysts [14,34,39,56]. As reported in literature, N1 can be coordinated with Fe [11,13,35,41,52], enlightening the formation of Fe–N moieties into the CNN samples, which should act as active sites for ORR.

From the wide scan XPS spectra analyses of all the Fe–N/CNNs, the predominant Fe oxidation state is +2, since only the Fe 2p peak is present (see Fig. S2 of SI). From the deconvolution of the high-resolution XPS spectra of Fe 2p, the coordination environments are of FeO, Fe₂O₃, Fe₃O₄ and FeCO₃ types, thus confirming that part of the iron is encapsulated into the carbon structure [57,58].

3.2. Electrochemical characterization

3.2.1. Rotating disk electrode

Electrochemical tests were performed by means of RDE. Fig. 6a shows the Faradaic current density curves of the prepared electrocatalysts. The ORR kinetic current I_k was calculated taking into account the mass transport correction by using the relationship established by the Koutecky–Levich (K–L) theory (see Eq. (1)) [59]:

$$I_k = \frac{I_F \cdot I_{lim}}{I_{lim} - I} \quad (1)$$

where I_F is the Faradic current, I_{lim} is the limiting current density and I is the measured current density. The Faradaic current was calculated by subtracting the current obtained during the

anodic sweep scan in the N₂-saturated electrolyte (capacitive current) to the current obtained in the potential sweep recorded in O₂-saturated electrolyte under the same experimental conditions [35,52,60,61].

Fig. 6b reports the values of I_k calculated at 800 mV for all the electrocatalysts synthesized, showing maximum performance for the electrocatalyst Fe–N/CNN3, which contains the highest Fe and Co amounts. Apparently, the presence of Co enhances the ORR activity (Table 1). As described before, the amount of Co immediately affects the graphitization of the carbon, hence the presence of defects, and thus the efficiency of nitrogen incorporation inside the carbon structure. The activity is also related to the quantity and type of nitrogen fixed to the carbon matrix and their respective amount of iron, as described by previous studies [31,36,42]. According to the literature, the electrocatalytic ORR activity can be attributed to the presence of N1 or N2 [7,35,50–52]. Interestingly, in our case, the best activity belongs to the sample with approximately the same content of N1 and N2 (36 and 28%, respectively), the Fe–N/CNN3 catalysts, whereas when the N1 and N2 are very unbalanced (when N1 is high, N2 is low, or vice versa; see Table 2), the electroactivity towards ORR is limited (see Fig. 6b).

The importance of the metallic site for ORR is questioned in the current literature [11,13,36,42,62,63]. There are two different opinions regarding the nature of the active sites as to whether the metal is an active participant in the ORR or not [42]. Many groups claim that transition metals such as Fe and Co are fundamental during heat treatment in creating active sites, fixing N in the carbon structure, but their role is not active in the ORR [5,42].

This hypothesis is difficult to prove but it is in agreement with our results, as shown in Fig. 6b. On the other hand, we find that the more active electrocatalyst is the one containing the highest

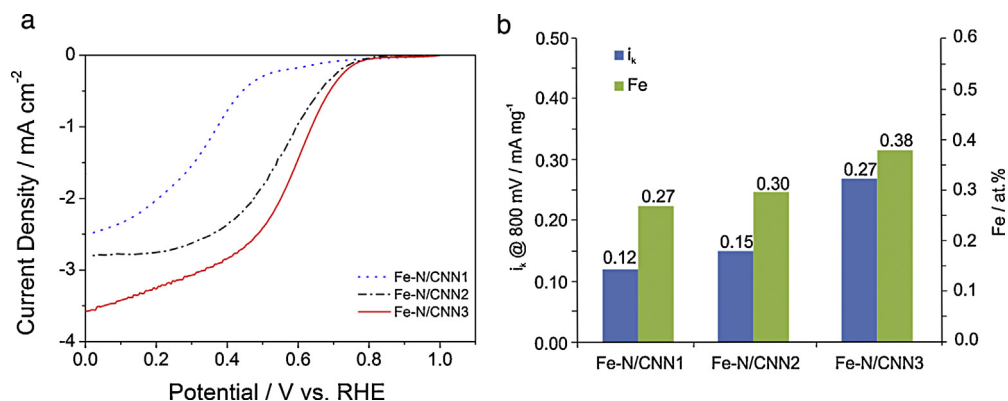


Fig. 6. (a) LSV curves for the ORR catalyzed by the synthesized electrocatalyst in O₂ saturated 0.5 M H₂SO₄ solution obtained with a potential scan rate of 10 mV s⁻¹ and electrode rotation rate of 1600 rpm. Catalyst loading 400 μg cm⁻². (b) Kinetic current measured at 800 mV normalized by mass capacitance from (a), Fe content from EDX analysis, Table 2, for the synthesized electrocatalysts.

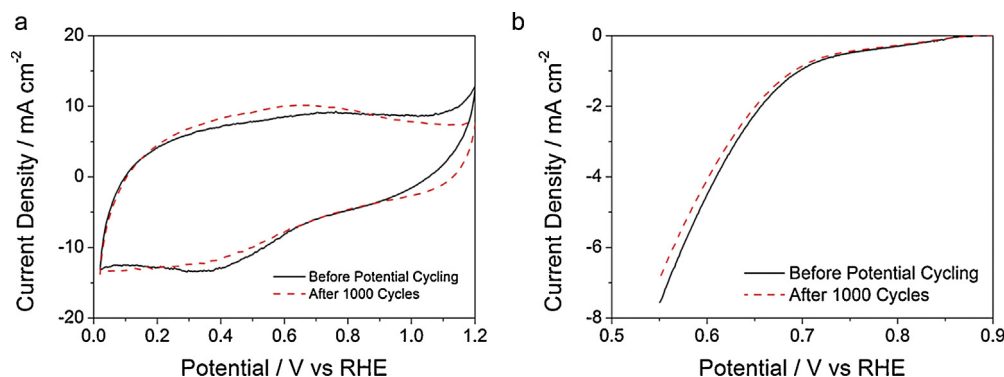


Fig. 7. (a) IR-corrected CV of Fe-N/CNN3 electrocatalyst after 1000 potential cycling, at room temperature in N₂-bubbled 0.5 H₂SO₄ solution at 50 mV s⁻¹. (b) IR-corrected polarization curves before and after 1000 cycles under O₂ under 10 mV s⁻¹.

amount of Fe and Co. This might be due either to the effect of Co on the amount of defects that favor binding of the nitrogen and thus the creation of active sites, or to a participation of Co in the ORR reaction mechanism through a synergy between Co and Fe-N complex [46,64,65]. The first hypothesis is supported by our results since the number of defects in the synthesized electrocatalysts is proportional to Cobalt content (see Table 1). The latter hypothesis is unlikely, since previous studies showed that bare CNN supports grown from transition metals do not have ORR activity [26].

According to the obtained results from the electrochemical screening, Fe-N/CNN3 can be considered as the best produced electrocatalysts, showing the higher activity (0.27 mA mg⁻¹). Thus, it has been selected for further analysis in PEMFC and DMFC.

3.2.2. Half-cell studies

Typically, carbon-supported catalysts are prone to rapid degradation in accelerated tests, showing durability issues which are also related to weak interactions between metal and carbon support. The use of nitrogen as a doping agent is expected to increase the bonding energy of the metal to the support [52,60,64,66,67]. Fe-N/CNN3 durability was tested in half-cell studies when cycling the potential between 0.6 and 1.2 V vs RHE for 1000 times. CVs before and after ADTs are reported in Fig. 7a. The ORR activity decreased due to potential cycling (see Fig. 7b). A relatively small activity decay, 10% at 800 mV vs RHE (from 0.30 to 0.27 mA cm⁻²), can be observed after 1000 cycles for the present sample. This can be explained by the high amount of quaternary nitrogen, N3, found in the electrocatalyst structure (see Table 2). In fact, previous studies showed that N3 is the most stable in acid conditions, while pyridinic and pyrrolic, N1 and N2, can undergo fast degradation [32,68].

3.3. Fuel cell tests

In hydrogen-fed PEMFC single-cell tests, we investigated the effect of temperature, reactants pressure, flow and stoichiometry. Higher pressure always produces an increase in both the open-circuit voltage (OCV) and maximum power. Higher temperatures increased the cell performance. A maximum power density of 121 mW cm⁻², corresponding to 47 mW mg_{cat}⁻¹, was achieved at 60 °C and 200 kPa relative pressure. The corresponding polarization and power density curves are shown in Fig. 8a and compared to the same curves measured at 30 °C. Measured performance values were higher than what was reported in similar studies, e.g. Bezera *et al.* achieved 70 mW cm⁻² corresponding to 14 mW mg_{cat}⁻¹ at 80 °C [12], Wang *et al.* achieved 80 mW cm⁻² corresponding to 10 mW mg_{cat}⁻¹ at 60 °C, Choi *et al.* [68] achieved 40 mW cm⁻² corresponding to 10 mW mg_{cat}⁻¹ at 80 °C.

Compared to the best state-of-the-art studies, the present results are lower but mostly of the same order of magnitude [14,15,21,36,43]. Recently, Lefevre *et al.* [14], Wu *et al.* [15] and Cheon *et al.* [21] obtained the highest performance reported so far at 80 °C, 280 mW cm⁻² corresponding to 280 mW mg_{cat}⁻¹, 550 mW cm⁻² corresponding to 138 mW mg_{cat}⁻¹, 700 mW cm⁻² corresponding to 460 mW mg_{cat}⁻¹, respectively.

In DMFC single-cell tests, we investigated the effect of temperature, reactants pressure, flow and stoichiometry as well as methanol concentration. Higher pressures increased performance and decreased OCV due to a higher methanol crossover. Higher temperatures increased the performance without significantly affecting the OCV. The best performance, 15 mW cm⁻², was achieved at 90 °C, 2 bar, 0.1 NLPM O₂, 2 mL min⁻¹ MeOH at 2 M (Fig. 8b). The obtained performance values were of the same order

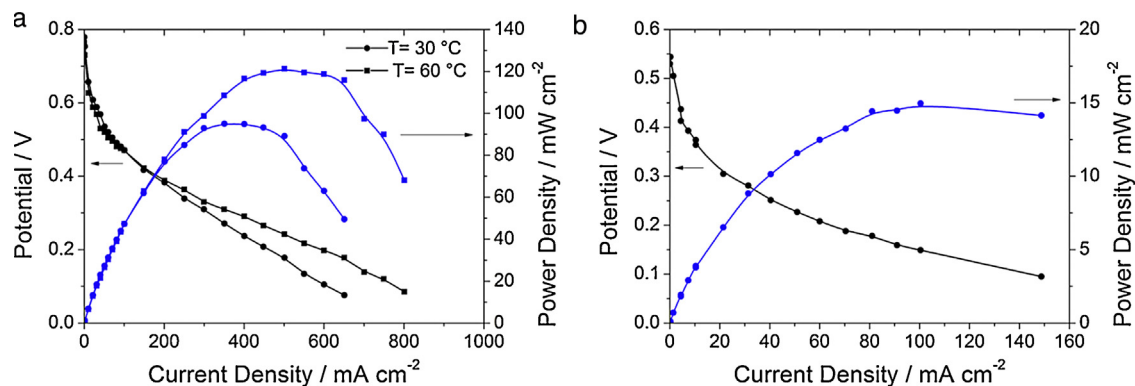


Fig. 8. Polarization and power density curves: (a) in H₂ single cell at 30 and 60 °C, 0.1 NLPM H₂, 0.2 NLPM O₂; (b) in MeOH single cell, 2 M methanol as anode feed, 0.1 NLPM O₂ and 90 °C.

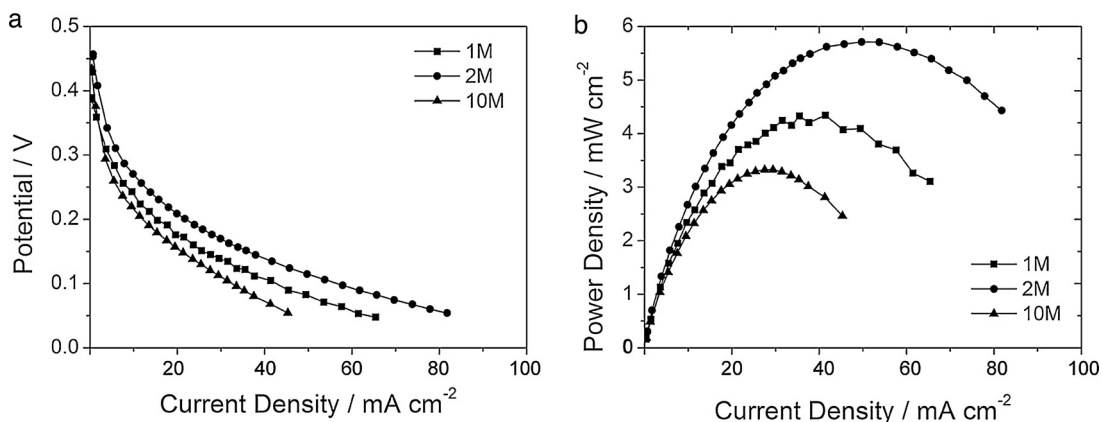


Fig. 9. (a) Polarization and (b) power density curves in MeOH single cell, 1, 2 or 10 M methanol as anode feed, 0.1 NLPM O₂ and 60 °C.

of magnitude as in similar recent studies, e.g. Wei *et al.* [69], taking into account the different catalyst loading.

Fig. 9a and b shows polarization curves and power density curves, respectively, at 60 °C for different methanol concentrations. Previous studies showed that nitrogen-doped graphitic structures are more methanol-tolerant than Pt-based catalysts [70]. Generally, higher methanol concentrations in the feed decrease the performance. However, in our study, a higher performance was achieved with a 2 M methanol concentration. Most likely, 2 M methanol concentration represents the optimum compromise between faster kinetics and methanol cross-over that have opposite effects on performance.

4. Conclusion

Three Fe–N non-noble electrocatalysts were synthesized using networked graphitic structures as support and were tested for the ORR. Interestingly, electrochemical tests showed that the best performance was obtained with the catalyst presenting the highest amount of Fe and Co and the highest amount of defects. This was attributed to the influence of Co on morphology, graphitization and level of disorder, and thus on the efficiency of nitrogen introduction in the carbon structure. Durability to potential cycling presented a relatively small activity loss of 10% after 1000 cycles due to the enhanced stability produced by the presence of quaternary nitrogen. The best performing electrocatalyst, Fe–N/CNN3, was tested in both PEMFC and DMFC. The maximum power achieved in single-test cells, 121 and 15 mW cm⁻², respectively, was either superior than or of the same order of magnitude of the performance reported in literature for similar catalysts. The simplicity of the synthesis procedure and the low material costs make the present systems an interesting alternative to state-of-the-art Pt-based electrocatalysts.

Acknowledgments

The authors acknowledge financial support from the Advanced Dutch Energy Materials (ADEM) innovation lab, from the COST CM1101 Action, and from the Italian Ministry of Education and Universities (MIUR) funding the PRIN 2010–2011 project NAMED-PEM (“Advanced nanocomposite membranes and innovative electrocatalysts for durable polymer electrolyte membrane fuel cells”, protocol n. 2010CYTWAW).

Appendix A. Supplementary data

Supplementary data associated with this article can be found, in the online version, at <http://dx.doi.org/10.1016/j.apcatb.2014.10.074>.

References

- [1] R. Dillon, S. Srinivasan, A.S. Aricò, V. Antonucci, *Journal of Power Sources* 127 (2004) 112–126.
- [2] S. Specchia, C. Francia, P. Spinelli, *Polymer Electrolyte Membrane Fuel Cells, Electrochemical Technologies for Energy Storage and Conversion*, Wiley-VCH, Weinheim, Germany, pp. 601–670.
- [3] F.A. de Bruijn, V.A.T. Dam, G.J.M. Janssen, *Fuel Cells* 8 (2008) 3–22.
- [4] R.K. Ahluwalia, X. Wang, J. Kwon, A. Rousseau, J. Kalinoski, B. James, J. Marcinkoski, *Journal of Power Sources* 196 (2011) 4619–4630.
- [5] F. Jaouen, E. Proietti, M. Lefevre, R. Chenitz, J.-P. Dodelet, G. Wu, H.T. Chung, C.M. Johnston, P. Zelenay, *Energy and Environmental Science* 4 (2011) 114–130.
- [6] J.A.R. van Veen, J.F. van Baar, K.J. Kroese, *Faraday Transactions 1: Physical Chemistry in Condensed Phases* 77 (1981) 2827–2843.
- [7] D. Scherson, A.A. Tanaka, S.L. Gupta, D. Tryk, C. Fierro, R. Holze, E.B. Yeager, R.P. Lattimer, *Electrochimica Acta* 31 (1986) 1247–1258.
- [8] K. Wiesener, D. Ohms, V. Neumann, R. Franke, *Materials Chemistry and Physics* 22 (1989) 457–475.
- [9] Z. Chen, D. Higgins, A. Yu, L. Zhang, J. Zhang, *Energy and Environmental Science* 4 (2011) 3167–3192.
- [10] G. Lalonde, C. Faubert, R. Côté, D. Guay, J.P. Dodelet, L.T. Weng, P. Bertrand, *Journal of Power Sources* 61 (1996) 227–237.
- [11] F. Jaouen, M. Lefèvre, J.-P. Dodelet, M. Cai, *The Journal of Physical Chemistry B* 110 (2006) 5553–5558.
- [12] C.W.B. Bezerra, L. Zhang, K. Lee, H. Liu, J. Zhang, Z. Shi, A.L.B. Marques, E.P. Marques, S. Wu, J. Zhang, *Electrochimica Acta* 53 (2008) 7703–7710.
- [13] M. Lefèvre, J.P. Dodelet, P. Bertrand, *The Journal of Physical Chemistry B* 104 (2000) 11238–11247.
- [14] M. Lefèvre, E. Proietti, F. Jaouen, J.-P. Dodelet, *Science* 324 (2009) 71–74.
- [15] G. Wu, K.L. More, C.M. Johnston, P. Zelenay, *Science* 332 (2011) 443–447.
- [16] E. Proietti, F. Jaouen, M. Lefèvre, N. Larouche, J. Tian, J. Herranz, J.-P. Dodelet, *Nature Communications* 2 (2011) 416.
- [17] A. Ishihara, Y. Ohgi, K. Matsuzawa, S. Mitsushima, K.-I. Ota, *Electrochimica Acta* 55 (2010) 8005–8012.
- [18] A. Serov, M.H. Robson, K. Artyushkova, P. Atanassov, *Applied Catalysis B: Environmental* 127 (2012) 300–306.
- [19] A. Serov, U. Tylus, K. Artyushkova, S. Mukerjee, P. Atanassov, *Applied Catalysis B: Environmental*, 150–151 (2014) 179–186.
- [20] J.H. Zagal, F. Javier Recio, C.A. Gutierrez, C. Zuñiga, M.A. Páez, C.A. Caro, *Electrochemistry Communications* 41 (2014) 24–26.
- [21] J.Y. Cheon, T. Kim, Y. Choi, H.Y. Jeong, M.G. Kim, Y.J. Sa, J. Kim, Z. Lee, T.-H. Yang, K. Kwon, O. Terasaki, G.-G. Park, R.R. Adzic, S.H. Joo, Ordered mesoporous porphyrinic carbons with very high electrocatalytic activity for the oxygen reduction reaction, *Sci. Rep.* 3 (2013) 2715.
- [22] M. Ferrandon, X. Wang, A.J. Kropf, D.J. Myers, G. Wu, C.M. Johnston, P. Zelenay, *Electrochimica Acta* 110 (2013) 282–291.
- [23] R. Borup, J. Meyers, B. Pivovar, Y.S. Kim, R. Mukundan, N. Garland, D. Myers, M. Wilson, F. Garzon, D. Wood, P. Zelenay, K. More, K. Stroh, T. Zawodzinski, J. Boncella, J.E. McGrath, M. Inaba, K. Miyatake, M. Hori, K. Ota, Z. Ogumi, S. Miyata, A. Nishikata, Z. Siroma, Y. Uchimoto, K. Yasuda, K.I. Kimijima, N. Iwashita, *Chemical Reviews* 107 (2007) 3904–3951.
- [24] D. Sebastián, M.J. Lázaro, I. Suelves, R. Moliner, V. Baglio, A. Stassi, A.S. Aricò, *International Journal of Hydrogen Energy* 37 (2012) 6253–6260.
- [25] D. Sebastián, A.G. Ruiz, I. Suelves, R. Moliner, M.J. Lázaro, V. Baglio, A. Stassi, A.S. Aricò, *Applied Catalysis B: Environmental* 115–116 (2012) 269–275.
- [26] E. Negro, M.A.D. Vries, R. Latsuzbaia, G.J.M. Koper, *Fuel Cells* 14 (2014) 350–356.
- [27] K.N.K. Kowligi, G.J.M. Koper, R.A.D. Van Raalten, *Carbon nanostructures and networks produced by chemical vapor deposition*, Delft University of Technology, 2012.
- [28] K. Kowligi, U. Lafont, M. Rappolt, G. Koper, *Journal of Colloid and Interface Science* 372 (2012) 16–23.
- [29] E. Negro, R. Latsuzbaia, G.J.M. Koper, *Langmuir* 30 (2014) 8300–8307.

- [30] E. Negro, M. Dieci, D. Sordi, K. Kowlgi, M. Makkee, G.J.M. Koper, *Chemical Communications* 50 (2014) 11848–11851.
- [31] A.H.A. Monteverde Videla, L. Zhang, J. Kim, J. Zeng, C. Francia, J. Zhang, S. Specchia, *Journal of Applied Electrochemistry* 43 (2013) 159–169.
- [32] A.H.A. Monteverde Videla, S. Ban, S. Specchia, L. Zhang, J. Zhang, *Carbon* 76 (2014) 386–400.
- [33] L. Zhang, J. Kim, E. Dy, S. Ban, K.-C. Tsay, H. Kawai, Z. Shi, J. Zhang, *Electrochimica Acta* 108 (2013) 480–485.
- [34] L. Zhang, J. Kim, E. Dy, S. Ban, K.-C. Tsay, H. Kawai, Z. Shi, J. Zhang, *Electrochimica Acta* 108 (2013) 814–819.
- [35] H.R. Byon, J. Suntivich, Y. Shao-Horn, *Chemistry of Materials* 23 (2011) 3421–3428.
- [36] G. Liu, X. Li, P. Ganesan, B.N. Popov, *Electrochimica Acta* 55 (2010) 2853–2858.
- [37] J.-z. Zou, X.-r. Zeng, X.-b. Xiong, H.-l. Tang, L. Li, Q. Liu, Z.-q. Li, *Carbon* 45 (2007) 828–832.
- [38] P.K. Chu, L. Li, *Materials Chemistry and Physics* 96 (2006) 253–277.
- [39] F. Jaouen, A.M. Serventi, M. Lefèvre, J.-P. Dodelet, P. Bertrand, *The Journal of Physical Chemistry C* 111 (2007) 5971–5976.
- [40] H.R. Byon, J. Suntivich, E.J. Crumlin, Y. Shao-Horn, *Physical Chemistry Chemical Physics* 13 (2011) 21437–21445.
- [41] F. Charretre, F. Jaouen, S. Ruggeri, J.-P. Dodelet, *Electrochimica Acta* 53 (2008) 2925–2938.
- [42] J.-P. Dodelet, in: M. Shao (Ed.), *Electrocatalysis in Fuel Cells*, Springer, London, 2013, pp. 271–338.
- [43] J. Tian, A. Morozan, M.T. Sougrati, M. Lefèvre, R. Chenitz, J.-P. Dodelet, D. Jones, F. Jaouen, *Angewandte Chemie International Edition* 52 (2013) 6867–6870.
- [44] K. Lee, L. Zhang, H. Lui, R. Hui, Z. Shi, J. Zhang, *Electrochimica Acta* 54 (2009) 4704–4711.
- [45] K.I. Ozoemena, S.A. Mamuru, T. Fukuda, N. Kobayashi, T. Nyokong, *Electrochemistry Communications* 11 (2009) 1221–1225.
- [46] S. Li, L. Zhang, J. Kim, M. Pan, Z. Shi, J. Zhang, *Electrochimica Acta* 55 (2010) 7346–7353.
- [47] C.H. Choi, S.H. Park, S.I. Woo, *Applied Catalysis B: Environmental* 119–120 (2012) 123–131.
- [48] J. Casanovas, J.M. Ricart, J. Rubio, F. Illas, J.M. Jiménez-Mateos, *Journal of the American Chemical Society* 118 (1996) 8071–8076.
- [49] K. Stańczyk, R. Dziembaj, Z. Piwowarska, S. Witkowski, *Carbon* 33 (1995) 1383–1392.
- [50] P.H. Matter, L. Zhang, U.S. Ozkan, *Journal of Catalysis* 239 (2006) 83–96.
- [51] F. Jaouen, J. Herranz, M. Lefèvre, J.-P. Dodelet, U.I. Kramm, I. Herrmann, P. Bogdanoff, J. Maruyama, T. Nagaoka, A. Garsuch, J.R. Dahn, T. Olson, S. Pylypenko, P. Atanassov, E.A. Ustinov, *ACS Applied Materials and Interfaces* 1 (2009) 1623–1639.
- [52] J. Herranz, F.d.r. Jaouen, M. Lefèvre, U.I. Kramm, E. Proietti, J.-P. Dodelet, P. Bogdanoff, S. Fiechter, I. Abs-Wurmbach, P. Bertrand, T.M. Arruda, S. Mukerjee, *The Journal of Physical Chemistry C* 115 (2011) 16087–16097.
- [53] R. Arrigo, M. Havecker, R. Schlögl, D.S. Su, *Chemical Communications* (2008) 4891–4893.
- [54] H. Niwa, K. Horiba, Y. Harada, M. Oshima, T. Ikeda, K. Terakura, J.-i. Ozaki, S. Miyata, *Journal of Power Sources* 187 (2009) 93–97.
- [55] C.-W. Tsai, M.-H. Tu, C.-J. Chen, T.-F. Hung, R.-S. Liu, W.-R. Liu, M.-Y. Lo, Y.-M. Peng, L. Zhang, J. Zhang, D.-S. Shy, X.-K. Xing, *RSC Advances* 1 (2011) 1349–1357.
- [56] B. Merzougui, A. Hachimi, A. Akinpelu, S. Bukola, M. Shao, *Electrochimica Acta* 107 (2013) 126–132.
- [57] A.P. Grosvenor, B.A. Kobe, M.C. Biesinger, N.S. McIntyre, *Surface and Interface Analysis* 36 (2004) 1564–1574.
- [58] M. Descostes, F. Mercier, N. Thomat, C. Beaucaire, M. Gautier-Soyer, *Applied Surface Science* 165 (2000) 288–302.
- [59] C. Song, J. Zhang, in: J. Zhang (Ed.), *EM Fuel Cell Electrocatalysts and Catalyst Layers*, Springer, London, 2008, pp. 89–134.
- [60] X. Li, B.N. Popov, T. Kawahara, H. Yanagi, *Journal of Power Sources* 196 (2011) 1717–1722.
- [61] F.J. Pérez-Alonso, M.A. Salam, T. Herranz, J.L. Gómez de la Fuente, S.A. Al-Thabaiti, S.N. Basahel, M.A. Peña, J.L.G. Fierro, S. Rojas, *Journal of Power Sources* 240 (2013) 494–502.
- [62] W.Y. Wong, W.R.W. Daud, A.B. Mohamad, A.A.H. Kadhum, K.S. Loh, E.H. Majlan, *International Journal of Hydrogen Energy* 38 (2013) 9370–9386.
- [63] R. Othman, A.L. Dicks, Z. Zhu, *International Journal of Hydrogen Energy* 37 (2012) 357–372.
- [64] X. Fu, Y. Liu, X. Cao, J. Jin, Q. Liu, J. Zhang, *Applied Catalysis B: Environmental* 130–131 (2013) 143–151.
- [65] L. Ma, X. Shen, G. Zhu, Z. Ji, H. Zhou, *Carbon* 77 (2014) 255–265.
- [66] S. Kuroki, Y. Nabaie, M.-a. Kakimoto, S. Miyata, *ECS Transactions* 41 (2011) 2269–2276.
- [67] K. Niu, B. Yang, J. Cui, J. Jin, X. Fu, Q. Zhao, J. Zhang, *Journal of Power Sources* 243 (2013) 65–71.
- [68] J.-Y. Choi, R.S. Hsu, Z. Chen, *The Journal of Physical Chemistry C* 114 (2010) 8048–8053.
- [69] Y. Wei, C. Shengzhou, L. Weiming, *International Journal of Hydrogen Energy* 37 (2012) 942–945.
- [70] H.-P. Cong, P. Wang, M. Gong, S.-H. Yu, *Nano Energy* 3 (2014) 55–63.